Forward emission of positronium from nanochanneled silicon membranes

S. Mariazzi[1,2],* B. Rienäcker[3],* R. Magrin Maffei[4,5], L. Povolo[1,2], S. Sharma[2], R. Caravita[2], L. Penasa[1,2], P. Bettotti[1], M. Doser[3], and R. S. Brusa[1,2]

1]Department of Physics, University of Trento, via Sommarive 14, 38123 Povo, Trento, Italy
2]TIFPA/INFN Trento, via Sommarive 14, 38123 Povo, Trento, Italy
3]Physics Department, CERN, 1211 Geneva 23, Switzerland
4]Dipartimento di Scienze Fisiche Informatiche Matematiche, Università di Modena e Reggio Emilia, Via G. Campi 213/a, 41125 Modena, Italy
5]Istituto Nanoscienze-CNR, Via G. Campi 213/a, 41125 Modena, Italy

(Dated: March 7, 2022)

Positronium beam formation and manipulation are required in several fundamental experiments. Efficient positron/positronium conversion in transmission configuration would offer important geometrical advantages over the reflection one for these applications. A novel type of transmission positron/positronium converters, which consists of silicon membranes with pass-through nanochannels, was produced and tested. The amount of forward emitted positronium was studied as a function of the thickness of the membranes and the nanochannel size. A maximum of, at least, (16 ± 4) % of positrons implanted in (3.5 ± 0.5) μm thick membrane with nanochannel size of 5-8 nm were found to be forward emitted as positronium. A similar maximum amount of, at least, (16 ± 5) %, was found to be emitted from a membrane (7.7 ± 1.3) μm thick with nanochannel size of 7-10 nm. A preliminary evaluation shows that the maximum amount of forward emitted positronium with the entire kinetic energy distribution below 1 eV is, at least, 9 % of the positrons implanted in the (3.5 ± 0.5) μm thick membrane.

PACS numbers: 36.10.Dr, 78.70.Bj, 61.46.w

I. INTRODUCTION

Positronium (Ps) [1, 2] is the bound state of an electron and its antiparticle, the positron (e^+). This makes it the lightest purely leptonic matter/antimatter atom. It lends itself to a range of fields as a key testing ground for studies of quantum electrodynamics (QED) [3], astrophysics [4], and matter/antimatter symmetries [5]. Ps can exist in two ground states: the singlet state, para-positronium (p-Ps, total spin 0, formation probability 1/4) and the triplet state, ortho-positronium (o-Ps, total spin 1, formation probability 3/4). In vacuum, p-Ps decays into 2γ-rays with a mean lifetime of 125 ps, while o-Ps decays into 3γ-rays with a mean lifetime of 142 ns.
Ps can be obtained by implanting positrons with an energy of a few keV into solids [6, 7]. In metals and semiconductors, Ps can be formed only at the surface because, in the bulk, the electron density is such as to hinder a stable positron-electron bond [8]. On the opposite, in large band gap dielectrics, thanks to the reduced density of free electrons, Ps formation can occur also in the bulk [8, 9]. From such materials, both Ps formed in the bulk and reaching the surface and Ps formed directly at the surface can be emitted into vacuum [10]. Thanks to this double formation channel, silica has a high e^+/Ps conversion efficiency with an emission from its surface up to 84 % of the implanted e^+ [9]. By exploiting this silica characteristic, efficient sources of Ps have been recently developed by synthetizing either silica-based disordered porous systems [11–13] or oxidized nanochanneled silicon targets [14, 15]. These systems present a very high surface-area-to-volume ratio and a large fraction of implanted e^+ can be emitted into the cavities as Ps with a typical energy of the order of a few eV [10]. While p-Ps annihilates in a short time due to its reduced lifetime, o-Ps can diffuse along the interconnected cavities and eventually be emitted into the vacuum [13, 14]. In each collision with the surface of the cavity, Ps loses a fraction of its energy [16, 17] and Ps reaching the vacuum can have an energy significantly lower than the initial one [12, 15, 17–21]. In each collision there is the probability that Ps undergoes to the so called pick-off annihilation in which the e^+ of Ps annihilates with an electron of the medium [6]. Pick-off annihilations decrease the quantity of Ps out-diffusing into vacuum.

Up to now, most of the efforts have been focused on the realization of silica-based nanostructured e^+/Ps con-

* Corresponding authors: b.rienaecker@cern.ch, Mariazzi@science.unitn.it

Duration of the primary treatment							Detachment current and duration
3000 s	2300 s	1800 s	1400 s	1000 s	750 s	500 s	
Detachment	No detachment	No detachment					240 mA, 24 s
	Detachment	No detachment	No detachment				400 mA, 60 s
		Detachment	No detachment	No detachment			500 mA, 90s
			Detachment	No detachment	No detachment		1 A, 90s
				Detachment	No detachment	No detachment	2 A, 90s
					Detachment	No detachment	2.5 A, 90s
						Detachment	3 A, 30s

TABLE I. Burst current and time duration of the etching needed to detach a membrane with a surface larger than ∼(6 x 6) mm as a function of the duration time of the primary anodization. Successful detachment in white cells, tested no detachment in light grey cells and not tested combinations in dark grey cells.

verters in reflection geometry, i.e. Ps emitted from the same surface into which positrons are implanted [13, 14]. Only in recent years, first silica-based nanostructured e^+/Ps converters in transmission geometry (i.e. Ps emitted from the opposite side of the target with respect to the e^+ implantation) have been developed by deposition of an ultraporous silica thin film onto a 20 nm amorphous carbon foil [22–24]. Previously, small amounts of very fast Ps (kinetic energy of tens of eV) in transmission mode were achieved by employing gas cells [25, 26], C films [27] and Na-coated W thin films followed by photodetachment of the produced Ps^- [28].

The transmission geometry is very promising for all experiments where Ps has to be further transported and Ps beams have to be formed. For instance, this is the case of the use of Ps for the creation and studies of electron−positron plasmas in a stellarator [29], direct tests of the gravitational free-fall on Ps [30–34], and antihydrogen production via charge exchange reaction in which Ps atoms excited to Rydberg levels interact with an antiproton plasma [35–37]. However, the present transmission e^+/Ps converters [22] are not yet competitive with reflection targets in terms of Ps yield (fraction of Ps formed and emitted into the vacuum per implanted e^+) and Ps cooling. Until now, the yield of Ps in trasmission silica-based nanostructured targets was found to be up to ∼9 % while it is up to ∼45 % in reflection converters [23, 38]. The development of different types of transmission converters with higher yield would be beneficial for all the above mentioned experiments.

In the present work, we study the Ps forward emission from a novel type of transmission e^+/Ps converters consisting of thin membranes with pass-through nanochannels. The Ps emission in transmission was observed and investigated via Positron Annihilation Spectroscopy (PAS). Depth profiled 3γ-2γ annihilation ratio measurements (3γ-PAS) were performed with a continuous e^+ beam to estimate the amount of forward emitted Ps. The thickness of the membranes was tuned between ∼ 3.5 μm and ∼ 24 μm, while the nanochannel size was tuned between 5-8 nm and 7-10 nm by subsequent oxidation and re-etching [14]. The thickness of the membranes and the nanochannel size were characterized via Scanning Electron Microscopy (SEM) measurements. Their densities were estimated via interferometric analysis.

II. EXPERIMENTAL

A. Transmission e^+/Ps converters

Transmission positron/positronium converters were synthetized by electrochemical etching of silicon p-type wafers (111) with resistivity 0.1-1.5 Ω cm. Porous layers of different thickness were produced by appling an etching current of 10 mA/cm^2 and varying the anodization time. At the end of the etching treatment the porous layers were detached from the substrate by appling a strong current burst that completely dissolves the bottom silicon layer surrounding the etched area [39, 40]. The burst of current produces an empty cavity at the between the porous layer and the underlying bulk silicon wafer without altering the overlying porous structure. The actual experimental parameters to detach the membranes heavily depend on chemo-physical details (eg. silicon doping and orientation, porosity of the already etched region, composition of the etching solution). Once they are fixed, a reliable strategy can be derived using the approach detailed in Ref.[41]. After detaching, membranes with pass-through nanochannels with different thickness are obtained. The etching solution was realized by adding absolute ethanol to a commercial aqueous solution at 48 % of HF with a volume ratio of 1 : 3 = HF : ethanol. The anodization was performed at room temperature. Several membranes were produced by varying the anodization time from 500 s up to 3000 s. The anodization time is expected to be the most important parameter in the

determination of the thickness of the porous layer [42]. The current of the burst used for the detachment was varied between 240 mA and 3 A and its time duration between 24 s and 90 s, depending on the primary etching time (see TABLE I). The burst values have been carefully chosen to guarantee the detachment of membranes with a surface larger than around (6 x 6) mm. The detached membranes were then laid on a grating with 90 % of transparency, cleaned in absolute ethanol $\geqslant$ 99.8 % and oxidized in air at 100 °C for 2 hours. As demonstrated in previous works [15, 21], a fine tuning of the nanochannel diameter can be obtained by different number of etchings in the HF solution for 1 minute and re-oxidation in air at 100 °C for 2 h. Each etching process introduces tensile stresses on the membrane that can fragment the sample [43]. The survival of the membranes to the re-etching and re-oxidation cycles was tested. Membranes produced with an anodization time longer than 750 s survived to a single re-etching and re-oxidation cycle. Only the target anodized for 3000 s survived to the second re-etching and re-oxidation cycle.

B. 3γ-2γ annihilation ratio measurements

The Ps formation and Ps emission into vacuum were studied via 3γ-2γ annihilation ratio spectroscopy performed with a continuous positron beam [44]. With this technique it is possible to extract, as a function of the positron implantation energy, E, the fraction $F_{3\gamma}(E)$ of e^+ stopped by the target forming Ps and annihilating into 3γ. The depth profiling of the fraction $F_{3\gamma}(E)$ was carried out by implanting in the grounded target positrons with energy ranging from 1.5 to 26 keV. A high purity germanium detector (HPGe) placed at a distance of 3.5 cm from the targets was used to detect the gamma rays generated by direct e^+ annihilations and Ps annihilations. The efficiency of the HPGe detector was 45 % while its energy resolution at 511 keV was 1.4 keV [45]. The distribution of the annihilation γ-ray energy (E_γ) was subdivided into two regions: the 511 keV peak area (P) prevalently ascribable to 2γ annihilations ($|511 - E_\gamma| \leq 4.25$ keV) and the valley area (V), given by o-Ps 3γ annihilations ($410 \leq E_\gamma \leq 500$ keV). At least three spectra were acquired for each energy; the average $P(E)$ and $V(E)$ parameters were calculated and the standard deviation was set as error bar. The 3γ -2γ ratio of Ps, $R(E) = V(E)/P(E)$ parameter, was calculated as the ratio between the valley area and the peak area at each positron implantation energy E. The $R(E)$ parameter was calibrated by measuring the Ps formation in a Ge crystal at 1000 K [45–47]. The calibrated fraction of positrons implanted in the target annihilating as o-Ps is given by the equation [45, 47, 48]:

$$F_{3\gamma}(E) = \frac{3}{4}\left[1 + \frac{P_1(R_1 - R(E))}{P_0(R(E) - R_0)}\right]^{-1} \quad (1)$$

where R_1 (100 % positronium formation) is the value obtained by extrapolating to zero implantation energy the $R(E)$ curve measured in Ge held at 1000 K. R_0 (0 % positronium formation) is the value of $R(E)$ at the highest positron implantation energy: in the bulk of Ge, no Ps can be formed due to the high electron density. P_0 and P_1 are the values of the 511 keV peak area obtained at 0 % and 100 % Ps formation, respectively. The error in calibration, due to both 0 % and 100 % evaluation, was previously shown to cause only a small overestimation of $F_{3\gamma}(E)$ with respect to the actual Ps fraction. The error was evaluated to be less than 3.5 % [47]. The vacuum chamber, where the target was placed, had the same geometry in front of the target and behind it. The target was mounted in front of the HPGe detector, perpendicular to its surface and aligned with the center of the detector itself (see the Appendix for a schematic representation of the target region). With this geometry, the detector probes the region in front of the target and the one behind it with the same solid angle. Thanks to this symmetry, the calibration performed with the Ge crystal only measuring Ps emitted in reflection configuration holds also for Ps emitted in transmission. Positrons implanted in the targets quickly thermalize attaining a depth distribution that can be modeled in the first approximation by a Makhovian profile [49–53]:

$$P(z, E) = -\frac{d}{dz} e^{-\left(\frac{z}{z_0}\right)^2} \quad (2)$$

where z is the positron implantation depth and z_0 is a parameter defining the implantation profile shape in Makhov's parametrization that is related to the mean positron implantation depth $\bar{z}$ through the relation $z_0 = \frac{2\bar{z}}{\sqrt{\pi}}$. Finally, the mean positron implantation depth $\bar{z}$ (in nm) is related to the positron implantation energy, E (in keV), through the equation $\bar{z} = \frac{40}{\rho} E^{1.6}$, where ρ is the material density (in g/cm^3) [54]. Monte-Carlo simulations have recently shown the applicability of this Makhovian profile approximation to evaluate the positron implantation profile in nanochanneled silicon targets [53]. The density of bulk silicon is 2.33 g/cm^3 while the mass density ρ of the present membranes is decreased by the presence of nanochannels and it is evaluated with the method described in the next paragraph.

C. SEM pictures and interferometric analysis

The thickness of the converters was evaluated by acquisition of SEM images of the side of the detached membranes with a high resolution JEOL JSM-7001F thermal field emission Scanning Electron Microscope (SEM). SEM images of the surface of etched and re-etched samples were used to estimate the nanochannel size. To evaluate the surface area occupied by nanochannels, the software Fiji was used [55]. The nanochannels

are characterized by a reduction of the image brightness with respect to the not-etched surface and the software allowed to determine the occupied area with an error of 3 %, recognized as interval of typical brightness for nanochannels.

The density of etched and re-etched membranes was estimated from interferometric analysis using a Cary5000 instrument equipped with the near normal reflectance tool. From the (baseline-corrected) reflectance spectra, the optical thickness (nd) is measured, where n is the sample refractive index and d is the membrane physical thickness. Spectra were acquired in the visible range (800-300 nm) and the optical thickness was calculated as the average value from multiple periods (at least 6). nd is given by the equation:

$$d = \frac{N}{2W(n^2 - (sin\theta)^2)^{0.5}} \qquad (3)$$

that can be approximated to normal incidence to $nd = N/(2W)$, given the small incline of the beam ($\theta = 5°$). In the equation, N represents the number of considered periods and W is the wavenumber spectral region spanned by N. The refractive index of the membrane was calculated by deviding the measured optical thickness by the sample thickness known from SEM pictures. The density of the membrane is then derived using Bruggeman approximation: $n = n_{air}f_{air} + n_{Si}(1 - f_{air})$, where f_{air} represents the fraction of porosity, $n_{air} = 1$ is the air refractive index, and $n_{Si} \sim 3.8$ the one of Silicon [56]. The density of the membrane is finally calculated as $(1 - f_{air})$ $\times$ 2.33 g/cm^3.

III. RESULTS AND DISCUSSION

A. Estimation of the membranes thickness and density

The SEM picture of the side of the membrane produced with 500 s of primary etching is reported, as an example, in Fig.1a. This membrane is (3.5 $\pm$ 0.5) μm thick. The reported uncertainty corresponds to the maximum semi-dispersion of the membrane thickness, which is not perfectly uniform alongside the layer. The error was evaluated for each membrane sampling a surface larger than (6 x 6) mm. The increase of the etching time makes the resulting membrane thicker (Fig.1b). In the thickest membranes, an augment of the thickness inhomogeneity was observed with a consequent increase of the associated error bar (Fig.1b). The average thicknesses and their maximum semi-dispersion as a function of the etching time are summarized in TABLE II.

Hereafter, the target will be labeled according to their average thickness. The SEM picture of the surfaces of 24 μm converters after one etching cycle and one re-etching cycle are reported in Fig.2. According to the pictures of Fig.2, the size of the nanochannels is on average between 5-8 nm and 7-10 nm for etched and one time re-etched samples, respectively.

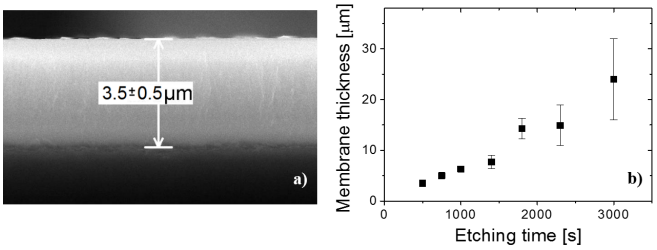

FIG. 1. Panel a), SEM image of the side of the membrane produced with an etching time of 500 s. The found distance between the front and the back surface is reported. The associated error corresponds to the maximum semi-dispersion of the thickness alongside the sample (see text). Panel b), behavior of the membrane thickness as a function of the etching time.

Interferometric analysis indicate a fraction of porosity f_{air}=0.46 $\pm$ 0.02 and f_{air}=0.52 $\pm$ 0.06 for etched and re-etched membranes, respectively. The corresponding densities are $(1-f_{air}) \times 2.33$ g/cm^3=1.3 $\pm$ 0.1 g/cm^3 and 1.1 $\pm$ 0.2 g/cm^3 for the etched and re-etched membranes, respectively.

Etching Time (s)	Thickness (µm)
500	3.5 ± 0.5
750	5.0 ± 0.3
1000	6.3 ± 0.2
1400	7.7 ± 1.3
1800	14.3 ± 2.0
2300	14.9 ± 4.0
3000	24 ± 8

TABLE II. Measured average membrane thickness as a function of the etching time. The associated error is represented by the maximum semi-dispersion.

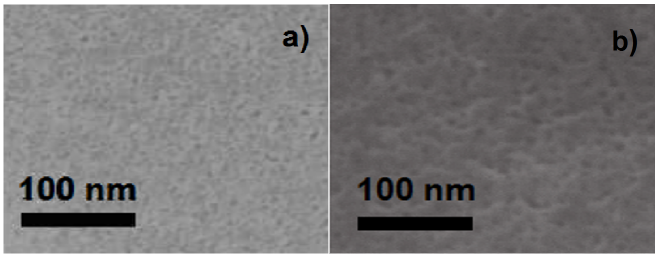

FIG. 2. SEM images of the surface of the targets produced with an etching time of 3000 s: panel a) etched sample and panel b) sample after one re-etching.

B. o-Ps fraction vs. membrane thickness

The fraction $F_{3\gamma}(E)$ of positronium annihilating via 3γ vs. positron implantation energy, E, is shown in Fig.3a for the thickest membranes produced with an

etching cycle ((14.3 ± 2.0) μm, (14.9 ± 4.0) μm, and (24 ± 8) μm). The reported error bars are statistical errors calculated by propagating the standard deviation on $R(E)$ parameter. $F_{3\gamma}(E)$ tops out at $E \sim$ 3-3.5 keV in the target of 24 μm and at around 2 keV in the membranes of 14.9 μm and 14.3 μm. At lower E, $F_{3\gamma}(E)$ shows a slight decrease coming from the combination of two processes: i) the presence of a lower Ps formation in the proximity of the front surface of the target due to Spur Ps formation process [57] and ii) the escaping from the nanochannels of Ps that experienced only few collisions with the nanochannels walls and hence with a high kinetic energy. A fraction of these Ps atoms travels a few centimeters away from the HPGe detectors before self-annihilation and some annihilation events are not detected. This is shown in detail in the Appendix where a Monte-Carlo study of the detection efficiency vs. Ps emission energy in our set-up is reported. The differences in the $F_{3\gamma}(E)$ at low energy in the three considered targets could be ascribable to a change in the characteristic of the sample surface, such as its roughness, due to the different time duration of the anodization process [58]. Above $E \sim$ 3 keV, the three $F_{3\gamma}(E)$ curves overlap pointing out the same structure (namely density and dimension) of the nanochannels. At growing energies, the three curves show a monotonic decrease due to the gradual increase of the Ps fraction annihilating via pick-off with an electron of the nanochannel walls. This causes the reduction of the Ps fraction able to back diffuse towards the front face of the membranes and be emitted into the vacuum. The behavior of the $F_{3\gamma}(E)$ curves of the thickest membranes is perfectly compatible with the one previously observed by measuring Ps in reflection geometry from nanochannels ending with a Si bulk substrate [14, 15, 21]. Indeed, Ps emission from the back surface of these thick membranes is expected to give a negligible contribution to the $F_{3\gamma}$ parameter for two concurring reasons. The first one is that, even at 26 keV of implantation energy, less than 3 % of positrons are expected to stop at a depth above 12 μm. The second one is related to the value of the Ps diffusion length. The diffusion length can be extracted by fitting the $F_{3\gamma}(E)$ curves, in the region of the monotonic decrease, with the diffusion model described in Ref.[14]. $F_{3\gamma}(E)$ data for E <3.5 keV were not considered in the fit because affected by the aforementioned influence of the front surface and presence of emitted undetected Ps (effects i) and ii)). The best fit of the $F_{3\gamma}(E)$ data measured in the target of 24 μm is reported in Fig.3a. It gives a diffusion lenght of (760 ± 80) nm. Within the errors, similar Ps diffusion length values were found by fitting the $F_{3\gamma}(E)$ curves of the 14.9 and 14.3 μm membranes. With this diffusion length, even Ps formed above 12 μm has low probability to reach the back surface of the membrane and escape into the vacuum. Althought the diffusion model used for the fit considers only Ps emitted in reflection and Ps annihilating via 3γ inside the nanochannels but no emission in transmission, the agreement between experimental data and the model reported in Fig.3a is very good. This gives an a posteriori confirmation that the amount of Ps emitted into vacuum from the back surface of these thick membranes is negligible.

The scenario changes if we observe the $F_{3\gamma}(E)$ curves measured in the thinnest membranes. In Fig.3b, the $F_{3\gamma}(E)$ curves measured in the membranes of 3.5 μm, 5.0 μm, 6.3 μm, and 7.7 μm are compared to the one corresponding to the target of 24 μm. In the target of 7.7 μm, the $F_{3\gamma}(E)$ curve follows the behavior of the ones of the thickest target up to around E = 13 keV. Between 13 keV and 20 keV, the curve shows higher values than the ones observed in 24 μm target pointing out an excess of 3γ annihilations that is consistent with Ps emitted from the back surface and annihilating into vacuum. For $E >$ 20 keV, the $F_{3\gamma}$ values drop below the ones measured in the 24 μm target. This behavior is due to a progressive increase of the fraction of implanted positrons that cross the membrane and by Ps emitted in transmission which fly away from the sample. These undetected events modify the proportion between counts in the valley, $V(E)$, and in the peak area, $P(E)$ (see section III.C). For targets thinner than 7.7 μm, the crossing of positrons through the membranes starts to be no more negligible. In the 7.7 μm target, it amounts to more than 20 % of e^+ implanted with an energy of 26 keV.

By reducing the thickness of the membrane, the Ps emission in transmission occurs at progressively lower positron implantation energy and its signal progressively increases. The vertical arrows in Fig.3b mark the central position of the excess in the $F_{3\gamma}$ signal for each membrane. In the membrane of 6.3 μm, the excess of 3γ annihilations is centered around E = 12 keV while it occurs at around E = 11 keV in the membranes of 5.0 μm and at ∼9.5 keV in the one of 3.5 μm. A quantification of the amount of Ps emitted in transmission (as well as in reflection at low E) cannot be obtained directly by the measured $F_{3\gamma}(E)$ curves without correcting them for the undetected fraction of Ps atoms [14]. In the next paragraph the method to correct the data is reported.

C. Correction of o-Ps fraction

The evaluation of the quantity of undetected Ps emitted from the targets, both in reflection and in transmission, can be obtained by analyzing the values of $P(E)$ and $V(E)$ measured in each membrane as a function of E [14].

In Fig.4, we report the sum of counts in the peak and in the valley areas in the unit of time, $P(E) + V(E)$, as measured in a virgin silicon sample and in the targets of 7.7 μm and 24 μm, chosen to represent membranes with and without Ps emission in transmission, respectively.

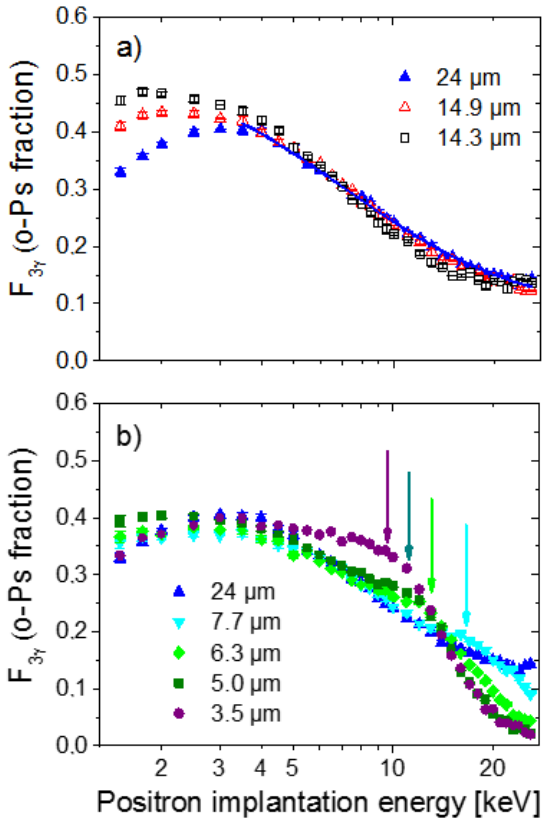

FIG. 3. Panel a): o-Ps, $F_{3\gamma}$, vs. positron implantation energy E for the membranes of 24 μm (up triangle), 14.9 μm (empty up triangle) and 14.3 μm (empty square). The continuous line through the points of the target of 24 μm is the best fit obtained by the diffusion model described in Ref.[14] (see text). Panel b): o-Ps, $F_{3\gamma}$, vs. positron implantation energy E for the membranes of 24 μm (up triangle), 7.7 μm (down triangle), 6.3 μm (diamond), 5.0 μm (square), and 3.5 μm (circle). The vertical arrows mark the excess of 3γ annihilations attributable to the Ps emission in transmission (see text). Statistical errors are reported.

Thanks to the flat transmission function of the apparatus [44], the $P(E)+V(E)$ values measured in silicon are constant in the used range of e^+ implantation energy. The $P(E)+V(E)$ curve measured in the membrane of 24 μm has a different behavior. It starts from very low values and then increases gradually with the increase of positron implantation energy. At high $E, P(E)+V(E)$ approaches a constant value slightly lower than the one observed in silicon. The loss of counts with respect to silicon is due to two effects:

a) gammas from 3γ Ps annihilations with E_γ out both of the selected peak and valley windows,

b) emission of Ps or positrons into the vacuum that fly away from the target and are detected with lower efficiency by the detector.

At low E, in the membrane of 24 μm, both a) and b) contribute to the loss of counts. On the opposite, at high energy, the effect a) is predominant because, due to the Ps diffusion length in the present nanochannels (see Sec.III.B), no emission of Ps flying far away from the target, neither from the front nor the back surface, can occur and no e^+ diffusion along the nanochannels into the vacuum is expected [14].

The $P(E)+V(E)$ curve measured in the target of 7.7 μm is similar to the one of the thickest membrane up to around 16 keV but, at higher E, the $P(E)+V(E)$ values start to decrease again. This deviation indicates the presence of both undetected Ps emitted in transmission and e^+ crossing the membrane.

Quantitatively, in a target with Ps formation, the counts in the peak and in the valley can be written as:

$$P(E) = P_{Si} - N_{escaped}(E) - N_{2\gamma 3\gamma}(E)$$
$$V(E) = V_{Si} + \frac{N_{2\gamma 3\gamma}(E)}{\alpha} \quad (4)$$

Where P_{Si} and V_{Si} are the constant values of the peak and valley areas measured in virgin silicon in the unit of time, $N_{2\gamma 3\gamma}(E)$ is the number of counts that disappear from the peak area due to 3γ Ps annihilations and α is a constant parameter which takes into account the fraction of $N_{2\gamma 3\gamma}(E)$ recorded in the valley area. Finally, $N_{escaped}(E)$ is the number of counts that disappear from the peak area due to undetected emitted Ps atoms or e^+.

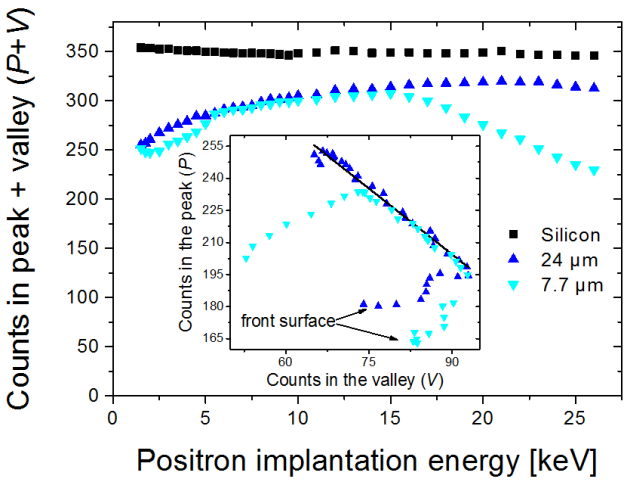

FIG. 4. Sum of the counts in the peak and in the valley area (P+V) in the unit of time vs. positron implantation energy as measured in a virgin silicon sample (square), in the target 24 μm (up triangle) and in the one 7.7 μm thick (down triangle). Inset: $P(E)$ vs. $V(E)$ curves in the unit of time measured in the membranes of 7.7 μm and 24 μm. The continuous line is the best fit of the linear part of the curve measured in the thickest target (see text). Statistical errors are smaller than the size of the symbols.

In the inset of Fig.4, we report the curves $P(E)$ vs. $V(E)$ measured in the membranes of 24 μm and 7.7 μm. In the case of the thickest membrane, for high positron implantation energy (roughly above 6 keV), all the data

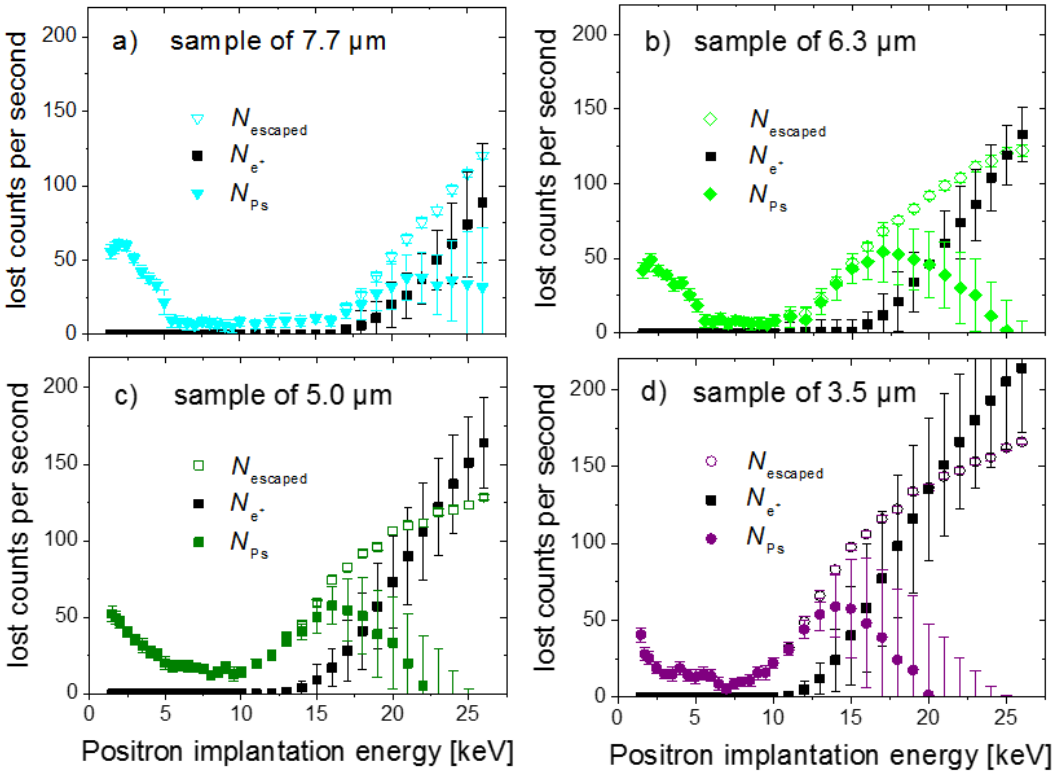

FIG. 5. Lost counts per second due to all the escape channels, $N_{escaped}(E)$, positrons crossing the membrane, $N_{e^+}(E)$, and undetected Ps atoms escaping from the target region, $N_{Ps}(E)$, for the target of 7.7 μm (panel a), 6.3 μm (panel b), 5.0 μm (panel c), and 3.5 μm (panel d) (see text). Statistical errors are reported.

lie along a straight line. This arises from the previously mentioned fact that, Ps formed deep in the nanochannels has very low probability to reach the surfaces of the membrane with high kinetic energy and no e^+ emission into the vacuum is expected. Consequently, $N_{escaped}(E)$ is negligible and, according to Eq.(4), one finds the linear relationship $P(E) = P_{Si} - \alpha V(E) + \alpha V_{Si}$. Fitting the linear part of the $P(E)$ vs. $V(E)$ curve, the term α can be evaluated as 2.05 $\pm$ 0.06. The two terms V_{Si} and P_{Si} are known from the measurement in virgin silicon and they amount to 45 $\pm$ 2 and 304 $\pm$ 2, respectively. Deviations of the $P(E)$ vs. $V(E)$ curve from the linearity, like the ones shown by the 7.7 μm target both at low and at high E, indicate the presence of $N_{escaped}(E) \neq 0$. By solving the system given by Eq.(4), one can obtain the lost counts per second:

$$N_{escaped}(E) = P_{Si} - P(E) - \alpha[V(E) - V_{Si}] \quad (5)$$

where $\alpha[V(E) - V_{Si}] = N_{2\gamma 3\gamma}(E)$.

The $N_{escaped}(E)$ curve for the target of 7.7 μm is reported in Fig.5a while the ones relative to the membranes of 6.3 μm, 5.0 μm and 3.5 μm are reported in the panels 5b, 5c, and 5d, respectively. The $N_{escaped}(E)$ curves have a similar behavior in all the thin membranes. The curves start from a value of around 50 counts per seconds at very low E then quickly decrease approaching zero counts per second for $E > 5$ keV. In principle, the signal at low E can be attributed to the emission in reflection of undetected Ps, the presence of backscattered positrons and the reemission of epithermal positrons. However, as discussed in Ref.[14], the last two contributions are expected to be negligible in our low Z - Si/SiO_2 systems. Thus, the $N_{escaped}(E)$ signal at low E is entirely ascribable to undetected Ps emitted in reflection.

From 5 keV up to 10-15 keV (depending on the thickness of the membrane), the $N_{escaped}(E)$ values are very low, pointing out neither backward or forward reemission of undetected Ps and e^+. Differently, at high E, $N_{escaped}(E)$ values show a quick increase. The amount of lost counts due to forward reemitted e^+ positrons, $N_{e^+}(E)$, can be estimated by integrating the Makhovian profile of Eq.(2) beyond the membrane thickness and normalizing for the maximum amount of two γ-ray decays that corresponds to the measured term P_{Si}. The number of undetected Ps can be estimated as:

$$N_{Ps}(E) = N_{escaped}(E) - N_{e^+}(E) \quad (6).$$

The $N_{e^+}(E)$ and $N_{Ps}(E)$ curves for the targets of 7.7 μm, 6.3 μm, 5.0 μm, and 3.5 μm are reported in Fig.5a, 5b, 5c, and 5d, respectively.

The reported errors on $N_{e^+}(E)$ come out from the un-

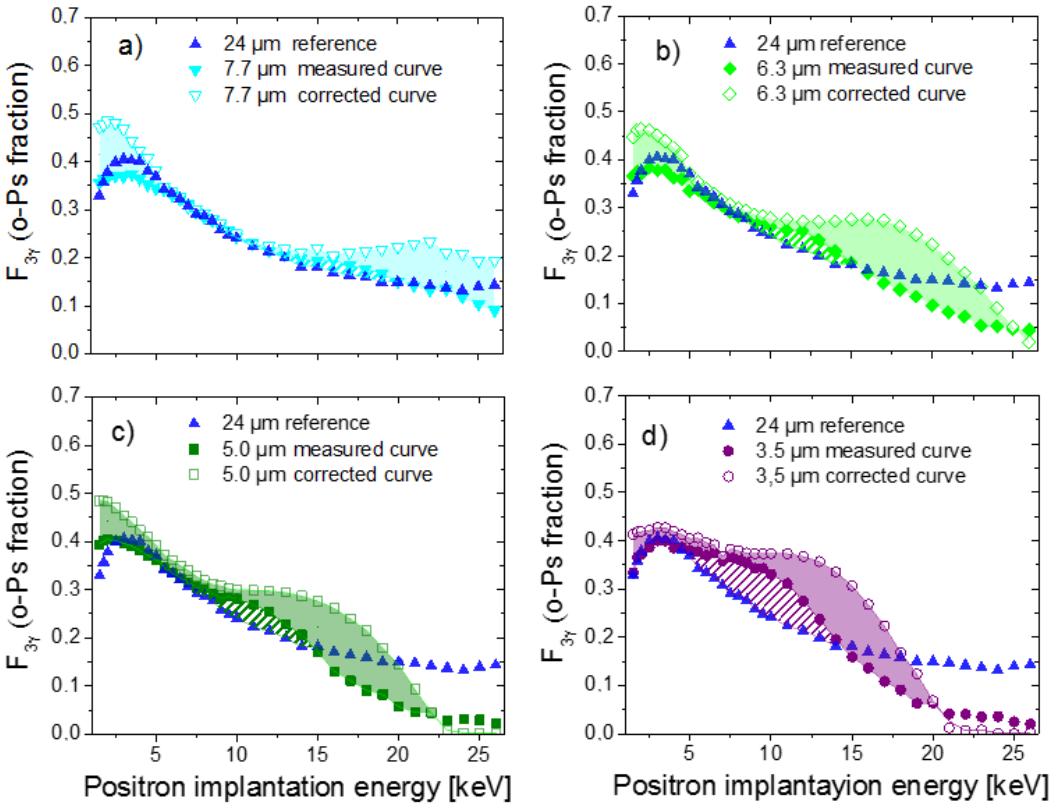

FIG. 6. $F_{3\gamma}(E)$ measured curves and $F_{3\gamma}(E)$ corrected curves for the target of 7.7 μm (panel a), 6.3 μm (panel b), 5.0 μm (panel c), and 3.5 μm (panel d). $F_{3\gamma}(E)$ corrected curves were calculated taking into account the presence of undetected Ps atoms, $N_{Ps}(E)$ (see text). The $F_{3\gamma}(E)$ curve measured in the target of 24 μm is reported as reference of a membrane without Ps emission in transmission. The homogeneous colored bands visually represent the excess of signal in each $F_{3\gamma}(E)$ corrected curve with respect to the corresponding measured one. The excess of signal of the $F_{3\gamma}(E)$ measured curve of each target with respect to the one of the 24 μm target is marked with a parallel lines pattern. See the text for the physical interpretation of the two regions. The error bars are not reported for clarity.

certainties on the thickness and the density of each membrane (see Sec.III.A) on the Makovian profile. The errors on $N_{Ps}(E)$ are the results of the propagation of the errors on $N_{e^+}(E)$ and $N_{escaped}(E)$. The $N_{e^+}(E)$ curves are null at low E and rise at high positron implantation energy. This rise starts at lower energy decreasing the membrane thickness. For high E in the two thinnest targets, N_{e^+} tends to be larger than $N_{escaped}$. This would indicate a slight underestimation of the measured values of the density or the thickness of these two membranes. However, the large errors on N_{e^+} at high E and the substantial compatibility of N_{e^+} and $N_{escaped}$ do not allow any strong statement. The $N_{Ps}(E)$ curves show value higher than zero below $E \sim 5$ keV pointing out the presence of undetected Ps backward emitted, in agreement with what is found in backscattering converters [14]. Between 5 keV and 12 keV, $N_{Ps}(E)$ value is close to zero and it increases again above $E = 12$ keV. This behavior is consistent with the forward emission of undetected Ps in addition to the detected fraction discussed in Sec.III.B. While in the thickest membrane $N_{Ps}(E)$ values show just a slight decrease at high E, in the thinnest ones $N_{Ps}(E)$ reaches a maximum before decreasing again. This maximum occurs at $E \sim 17$ keV, $E \sim 16$ keV, and $E \sim 14$ keV, for the targets of 6.3 μm, 5.0 μm, and 3.5 μm, respectively. The decrease in the $N_{Ps}(E)$ values is due to the increasing fraction of e^+ piercing the target, i.e. without the possibility to produce Ps.

By adding $N_{Ps}(E)$ counts, weighted by the term α, to the valley area in the $R(E)$ parameter, one can correct the measured $F_{3\gamma}(E)$ for the not detected Ps atoms. In Fig.6, we report the measured $F_{3\gamma}(E)$ curves and the corrected ones for the targets of 7.7 μm (panel a), 6.3 μm (panel b), 5.0 μm (panel c), and 3.5 μm (panel d). The $F_{3\gamma}(E)$ curve measured in the target 24 μm thick, that does not emit Ps in transmission, is reported as reference. The corrected $F_{3\gamma}(E)$ curves, including the not counted backward and forward escaping Ps, shows a slight increase of the values at low energy (below $E \sim 5$ keV) and a more evident increase at high energy with respect to the measured $F_{3\gamma}(E)$ curves. The amount and the dynamic of the increase at low e^+ implantation energy are quite similar in all the targets while the increase at high E is dependent on the thickness of the membrane and

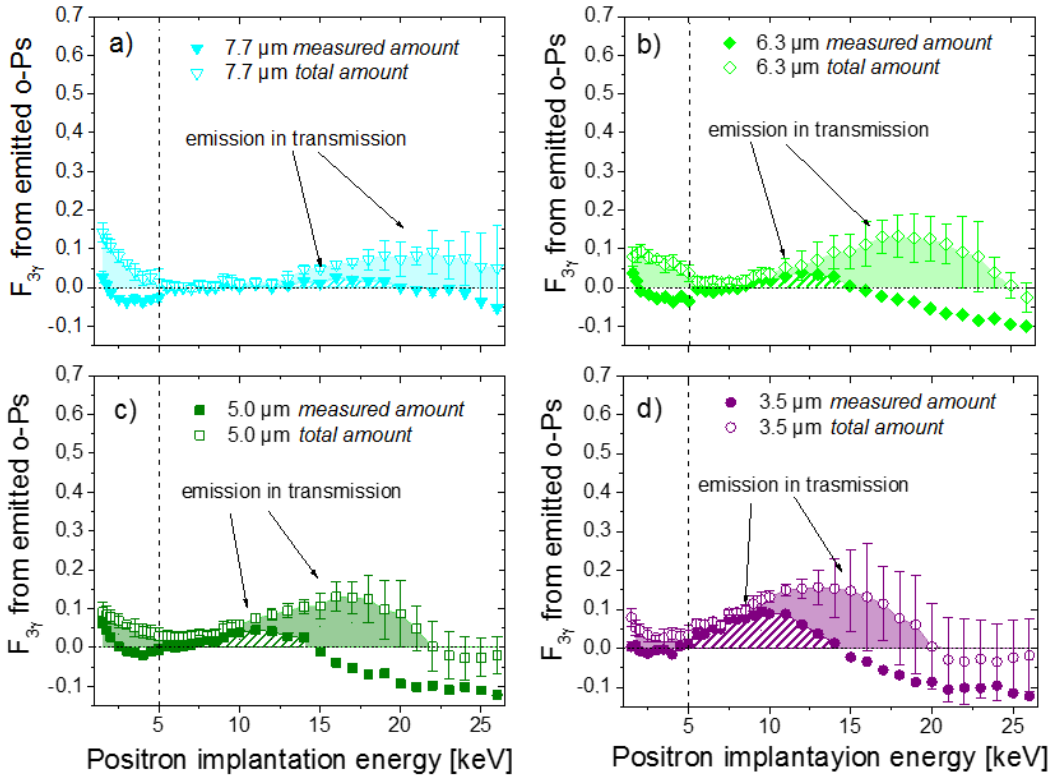

FIG. 7. *Measured* (full symbols) and *total amounts* (*measured* + *corrected amounts*) (empty symbols) of o-Ps 3γ annihilations generated by Ps emitted from the membranes of 7.7 μm (panel a), 6.3 μm (panel b), 5.0 μm (panel c), and 3.5 μm (panel d). The vertical lines mark the energy above which the contribution due to undetected Ps emitted in reflection vanishes and the entire signal can be ascribed to Ps emission in transmission. The *measured amount* of Ps emitted in transmission is marked with a parallel lines pattern while the *corrected amount* is marked with homogeneous color according to the code of Fig.6. Statistical errors are reported. See text for details.

starts at progressively lower E decreasing the thickness of the membrane. At higher e^+ implantation energy, the corrected $F_{3\gamma}(E)$ values show a decrease, that makes the curves approaching the measured curves. This decrease is due to the already discussed increase of e^+ crossing the target to the detriment of Ps formation (Fig.5).

D. Estimation of o-Ps emission in transmission

Let us now estimate the amount of Ps emitted in transmission from the present membranes. As seen in Sec.III.B, no forward Ps emission is expected from the target 24 μm thick. Thus, the $F_{3\gamma}$ values measured in this target at each E have to be enterely ascribed to Ps backward emitted and Ps annihilating via 3γ inside the nanochannels. The $F_{3\gamma}(E)$ curves measured in the thinnest targets present an excess of signal with respect to the one measured in the target 24 μm thick. This excess is attributable to the emission of Ps in transmission and it is marked with a parallel lines pattern in Fig.6. The amount of the marked region (in the following referred to as *measured amount*) has to be interpreted as a lower limit of the amount of forward emitted Ps because some Ps atoms, that at a given E annihilate via 3γ inside the nanochannels in the thick target, could reach the backward surface before self-annihilation being emitted in transmission from the thinnest targets. This contribution is expected to be negligible at low E where implanted positrons are at large distance from the back face of the target and becomes more important with the increase of E. For instance, according to Eq.(2), less than 0.1 % of e^+ implanted at $E = 5$ keV are beyond the half thickness of the 3.5 μm target, i.e. closer to the back face than the front one. At $E = 10$ keV, this fraction is around 20 % and only above $E = 13$ keV it reaches 50 %. Moreover, the $F_{3\gamma}(E)$ measured values do not take into account the undetected events, $N_{Ps}(E)$, discussed in the previous paragraph. The corrected $F_{3\gamma}(E)$ curves, calculated by considering also the lost counts, $N_{Ps}(E)$, are shown in Fig.6. The difference between the $F_{3\gamma}(E)$ curve with and without correction for each target represents the amount of undetected Ps emitted from the target both in reflection and in transmission. This amount is referred in the following as *corrected amount* and it is marked with a homogeneous coloration in Fig.6.

In Fig.7, we report the so found *measured amounts* of Ps emitted in transmission and the *total amounts*

(*measured+corrected amounts*) for each membrane. Also in this plot, the *measured amount* of Ps emitted in transmission is marked with a parallel lines pattern while the *corrected amount* is marked with homogeneous color.

As discussed in Sec.III.C, the effect of undetected Ps emitted in reflection vanishes above ∼5 keV. In Fig.7, a vertical dashed line marks this limit above which the behavior of the reported corrected curves has to be entirely attributed to Ps emission in transmission. The maximum *measured* and *total amounts* of forward emitted Ps and the corresponding positron implantation energies are summarized in TABLE III. The found values indicate that, both maximum *measured* and *total amount* increase by reducing the membrane thickness and in each membrane the peak of the *total amount* occurs at higher E with respect to the peak of the *measured* one. Both the results are consistent with the fact that, in transmission targets, Ps formed by positron implanted at low E has to travel a long path in the nanochannels to reach the back surface and it is eventually emitted into the vacuum with low energy, being detected by HPGe detector with a good efficiency. On the opposite, Ps formed by e^+ implanted with higher E has to travel for a shorter path in the nanochannels experiencing only an incomplete cooling. Consequently, they annihilate far from the target and some annihilation events are not detected (see Appendix). The curves in Fig.7 show that a significant amount of Ps is emitted in transmission by all the present membranes. The maximum amount of forward emitted Ps (at least (16 ± 4) %) is observed in the thinnest target.

Membrane	Maximum *measured amount* of forward emitted Ps [%]	E corresponding to the maximum *measured amount* [keV]	Maximum *total amount* of forward emitted Ps [%]	E corresponding to the maximum *total amount* [keV]
3.5 μm	9.4 ± 1.0	9.5	16 ± 4	13
5.0 μm	4.5 ± 0.4	11	13 ± 4	16
5.0 μm re-etched	5.2 ± 0.5	13	13 ± 6	15
6.3 μm	3.8 ± 0.5	12	13 ± 5	18
7.7 μm	2.6 ± 0.4	16	9 ± 5	22
7.7 μm re-etched	7.1 ± 0.7	15	16 ± 5	19

TABLE III. Maximum *total* and *measured amounts* of forward emitted Ps and corresponding positron implantation energies for the membranes of 3.5 μm, 5.0 μm, 6.3 μm, and 7.7 μm. The values for the membranes of 5.0 μm and 7.7 μm after re-etching and re-oxidation are also reported.

.

E. Effect of the nanochannel size enlargement on the Ps emission in transmission

As discussed in a previous work dealing with converters in reflection [14], the nanochannel size affects the Ps diffusion length and consequently the amount of Ps able to reach the target surface and being emitted into the vacuum. This is expected to be the case also for Ps emitted in transmission. In Fig.8a, we compare the $F_{3\gamma}(E)$ measured in the target of 24 μm (analyzed in detail in Sec.III.B and III.C) to the membrane produced with the same etching time but succesively re-etched and re-oxidized.

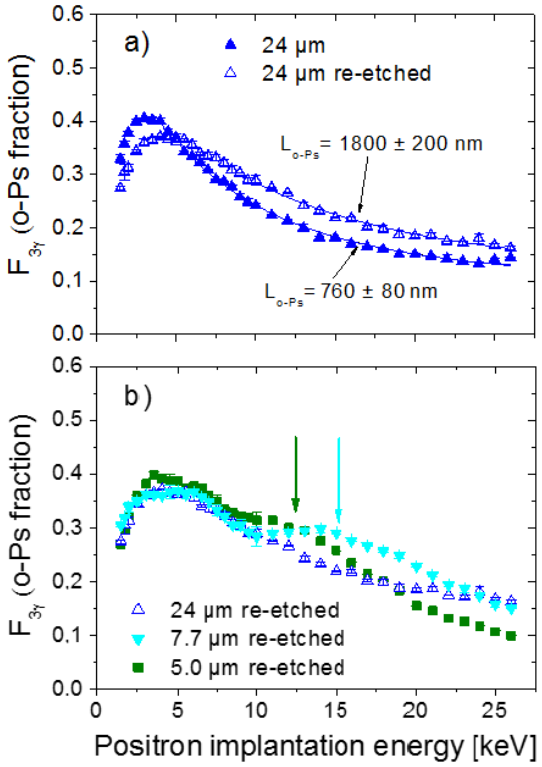

FIG. 8. Panel a): o-Ps fraction, $F_{3\gamma}$, vs. positron implantation energy E measured in the 24 μm membrane (up triangle) and the 24 μm membrane after re-etching and re-oxidation (empty up triangle). The continuous lines are the best fits obtained by the diffusion model described in Ref.[14] (see text). Panel b): o-Ps fraction, $F_{3\gamma}$, vs. positron implantation energy E measured in the membranes of 24 μm (empty up triangle), 7.7 μm (down triangle), and 5.0 μm (square) after re-etching and re-oxidation. The vertical arrows mark the excess of 3γ annihilations due to the Ps emission in transmission (see text). Statistical errors are reported.

The continuous lines are the best fits of the $F_{3\gamma}(E)$ curves in the region of monotonic decrease obtained with the diffusion model mentioned in Sec.III.B. A single re-etching and re-oxidation cycle increase the nanochannel size from 5-8 nm to 7-10 nm and a more than doubling of the Ps diffusion length from (760 ± 80) nm to (1800 ± 200) nm is observed. In Fig.8b, the $F_{3\gamma}(E)$ curves measured in the re-etched membranes of 24 μm, 7.7 μm and 5.0 μm (minimum thickness survived to a re-etching and re-oxidation cycle) are reported. As seen for etched targets (Fig.3b), also $F_{3\gamma}(E)$ curves of the thinnest re-etched membranes show an excess of 3γ annihilations with respect to the

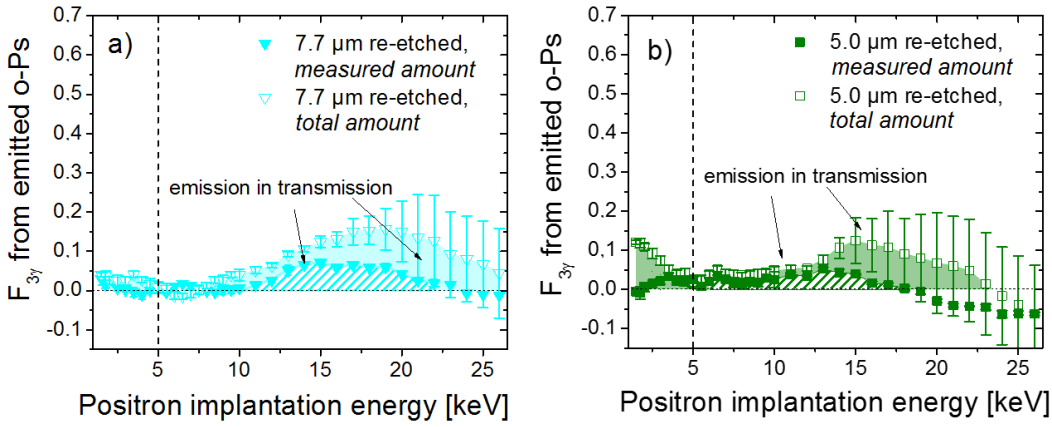

FIG. 9. *Measured amounts* (full symbols) and *total amounts* (*measured* + *corrected amounts*) (empty symbols) of o-Ps 3γ annihilations generated by Ps emitted from the membranes of 7.7 μm re-etched once (panel a) and 5.0 μm re-etched once (panel b). The vertical lines mark the energy above which the contribution due to fast Ps emission in reflection vanishes and all the signal can be ascribed to Ps emission in transmission. The *measured amount* of Ps emitted in transmission is marked with a parallel lines pattern while the *corrected amount* is marked with homogeneous color. Statistical errors are reported. See text for details.

$F_{3\gamma}(E)$ curve of the membrane 24 μm thick. These processes, consistent with Ps emission in transmission, occur at $E \sim 15$ keV in the target of 7.7 μm and at $E \sim 12$ keV in the one of 5.0 μm (see Fig.8b).

The procedure described in the previous sections was applied to estimate the *measured* and *corrected amounts* of Ps forward emitted by the re-etched targets. These amounts are reported in Fig.9a for the target of 7.7 μm and in Fig.9b for the target of 5.0 μm. The behavior of the *corrected* and *measured amounts* of o-Ps 3γ annihilations generated by Ps emitted from the re-etched membranes is similar to the ones observed in the not-re-etched ones. The maximum *measured* and *total amounts* of Ps forward emitted by these re-etched membranes are reported in TABLE III together with the corresponding positron implantation energies. Both the maximum *measured* and *total amounts* show a tendency to the increase with respect to the ones observed in the etched membranes with the same thickness. In particular, the maximum *measured amounts* of forward emitted Ps are moderately higher than the ones of the corresponding etched membranes of Fig.7. As these *measured amounts* are due to Ps slow enough to annihilate not far from the target, their increase could indicate that the size of nanochannels subjected to a re-etching cycle (7-10 nm) allows a more efficient forward emission of Ps with lower velocity. A rough evaluation, reported in the Appendix, shows that at least 9 %, 4 %, and 4 % of Ps atoms is forward emitted with an energy below 1 eV when positrons are implanted with an energy of around 9, 11, and 12 keV in the membranes 3.5, 5, and 6.3 μm thick, respectively. This amount is at least 5 % in the 5 μm re-etched membrane when positrons are implanted at energies of 13 keV. Doppler spectroscopy measurements of the $1^3S \rightarrow 2^3P$ [12, 21, 23, 59] would be necessary for characterizing the velocity spectrum of the forward emitted Ps. At the present, the bunched positron beam at our availability [60] does not allow this set of measurements due to the high E (larger than ~8 keV) required for the emission of Ps in transmission. Modifications of the positron bunching system to reach high e^+ implantation energy values [60] are under study.

IV. CONCLUSIONS

In the present work, we have investigated the Ps forward emission from a novel kind of transmission e^+/Ps converters: silicon membranes with thickness between 3.5 μm and 24 μm and with pass-through nanochannels (of size tuned between 5-8 nm and 7-10 nm) produced by electrochemical etching and detachment. Depth profiled 3γ-2γ annihilation ratio measurements pointed out evidences of Ps forward emission from membranes thinner than around (7.7 ± 1.3) μm while no Ps emission in transmission has been observed in thicker targets when e^+ are implanted with an energy up to 26 keV. From the thinnest membrane (3.5 ± 0.5) μm produced with nanochannel size of 5-8 nm, a maximum of, at least, (16 ± 4) % of e^+ in the target has been found to be emitted in transmission. A similar maximum amount, at least (16 ± 5) %, was found to be emitted from a membrane (7.7 ± 1.3) μm thick with nanochannel size of 7-10 nm. These values make the present targets almost two times more efficient than the e^+/Ps transmission converters available until now [23]. These values are lower than the ones observed in reflection, nevertheless the geometrical advantages offered by transmission configuration over the reflection one make the present membranes a promising option for all the applications where Ps transport is required.

A characterization of the kinetic energy of the Ps emitted

in transmission remains to be done. This is of great importance for the present membranes because the Ps forward emission is observed for high positron implantation energies, i.e. using positrons with a large implantation profile. Consequently, Ps atoms emitted in transmission are expected to exhibit a wide energy distribution.

ACKNOWLEDGMENTS

This work was supported by Q@TN, the joint lab between University of Trento, FBK- Fondazione Bruno Kessler, INFN- National Institute for Nuclear Physics and CNR- National Research Council and by the European Unions Horizon 2020 research and innovation programme under the Marie Sklodowska-Curie grant agreement No. 754496 FELLINI. The authors acknowledge Dr. N. Bazzanella for his kind availability for SEM measurements.

APPENDIX: MONTE-CARLO SIMULATIONS OF EMITTED POSITRONIUM

Monte-Carlo simulations were performed to study the detection efficiency of the Ps decay events within the geometry of our experimental chamber as a function of the Ps emission energy. A recently released simulation package based on the Geant4 toolkit and optimized for performing studies related to the different decay modes of positronium atoms [61] was used. The package allows studying the decays of Ps atoms under different environmental conditions, e.g., in vacuum or in materials, by providing the average lifetime of Ps atoms [62]. Fig.10 represents the schematic of the vacuum chamber used to perform the simulations. The formed Ps atoms are assumed to be emitted downward from the origin (0,0,0) within a total opening angle of 120° [63]. Two cylindrical housing cups made of aluminum with a radius of 4.5 cm, length of 10 cm and thickness 0.5 cm are placed on both sides of the origin with the bases at (±3 cm,0,0), respectively. Around these cups, two hollow cylindrical shields of 0.5 cm of tungsten are placed (grey cylinders in Fig.10). A HPGe crystal with a diameter of 6.2 cm and a length of 6.7 cm (dark cylinder in Fig.10) is encapsulated in the right hand side cup. The face of the detector is at 3.5 cm from the origin. A set of Monte-Carlo simulations was performed by changing the energies of the Ps atoms emitted in transmission in the range from 0.1 up to 10 eV [10]. o-Ps is assumed to amount to 3/4 of the total formed Ps while p-Ps is the remaining 1/4. Contrary to the short-lived p-Ps, the relatively long-lived o-Ps can fly away from the origin escaping from the detector view or reach the chamber walls.

The event-by-event fate of o-Ps atoms is simulated as follows:

- first, the emission angle of o-Ps in spherical coordinates was randomly selected: the angle ϕ was assumed to be within the azimuthal angle of 60° with respect to the y-axis. The polar angle Θ was simulated between 0 to 2π. The choise of the angle determines the line along which o-Ps travels.
- The velocity of the o-Ps atoms corresponding to a fixed o-Ps emission energy was calculated.
- A time-step of 0.5 ns was introduced.
- The fate of the o-Ps atom was tested at every time-step by comparing the probability of its decay for the fixed time-step in vacuum ($1 - e^{-0.5ns/142ns} = 0.0035$) with a randomly generated number in a uniform interval 0 to 1. If the generated number is smaller than the probability (0.0035), o-Ps atom annihilates into 3 photons.
- The total travel distance (r) was calculated using the time (summing over time steps) multiplied by the o-Ps velocity.
- Using the selected angles (ϕ, Θ) and r, the annihilation vertex was determined and its Cartesian coordinates (x,y,z) were calculated.
- The additional channel of the o-Ps atom decaying into 2 back-to-back annihilation photons due to the pick-off process was considered when the o-Ps reaches the walls of the experimental chamber before self-annihilation.

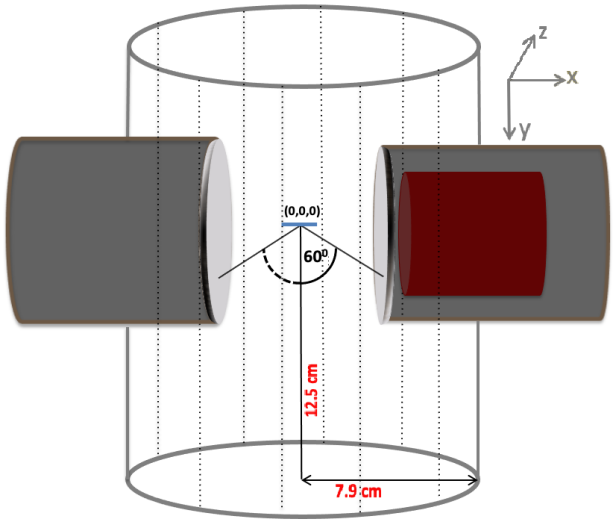

FIG. 10. Schematic representation of the target chamber with a radius of 7.9 cm. Positron beam is implanted from the top in the target shown as a horizontal line at the origin (0,0,0). Ps atoms emitted in transmission exit from the bottom of the target. The two aluminum cylindrical housing cups are represented in light grey and are surrounded by the two hollow cylindrical tungsten shields in dark gray. The HPGe detector (dark cylinder) is encapsulated in the cylindrical housing on the right.

The simulation of the spatial distribution of annihilation vertices of o-Ps atoms emitted with an energy of 5 eV is shown, as an example, in Fig.11. In the figure, red points represent the vertices of o-Ps self-annihilation via 3γ while blue points correspond to the positions of 2γ pick-off annihilations on the chamber walls.

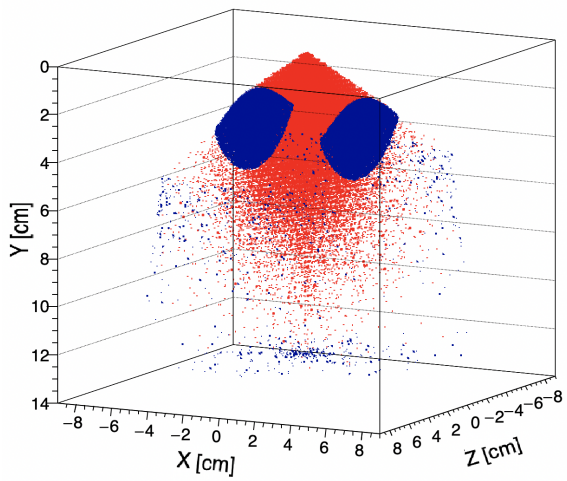

FIG. 11. Reconstructed vertices of the annihilation points of o-Ps atoms emitted with an energy of 5 eV. The red color shows the annihilation points of the o-Ps atoms decaying into 3γ while the blue color represents the vertices of the annihilation points of the o-Ps atoms on the obstacles along their trajectories. In this case, the o-Ps atoms are assumed to annihilate into two back-to-back 511 keV photons.

By knowing the annihilation vertex of each o-Ps atom, the decay channel (self-annilation in 3γ or pick-off annihilation in 2γ on the chamber walls) and the geometry of the detector region, the energy deposited in the HPGe by each annihilation event was simulated. In Fig.12, the energy deposition spectra computed assuming the annihilation of 10^8 Ps atoms (3/4 o-Ps and 1/4 p-Ps) with three different emission energies are reported. The red line shows the energy deposition spectra in the HPGe crystal for the Ps atoms emitted with a kinetic energy of 0.1 eV. The dash-dotted green and the blue dashed lines represent spectra for Ps atoms emitted with an energy of 5 eV and 10 eV, respectively. The energy deposition spectrum given by the annihilation of 10^8 positrons in the target was also simulated and it is shown as a black line.

The decrease (increase) of the counts in the valley area (peak area) with the increase of the Ps kinetic energy reflects the presence of o-Ps atoms escaping from the view of the detector (annihilating via pick-off on the chamber walls). The 3γ -2γ ratio of Ps, R parameter (see section II.A), was calculated as the ratio between the valley and the peak areas of the simulated spectra as a funtion of the Ps energy (E_{Ps}). The curve $(R(E_{Ps}) - R_0)/(R_1 - R_0)$ is shown in Fig.13. R_0 and R_1 are the normalization terms calculated as the V/P ratios in the spectrum without Ps formation and in the spectrum with the lowest Ps emission energy (i.e. with 100 % of Ps formation and a negligible fraction of not detected Ps), respectively.

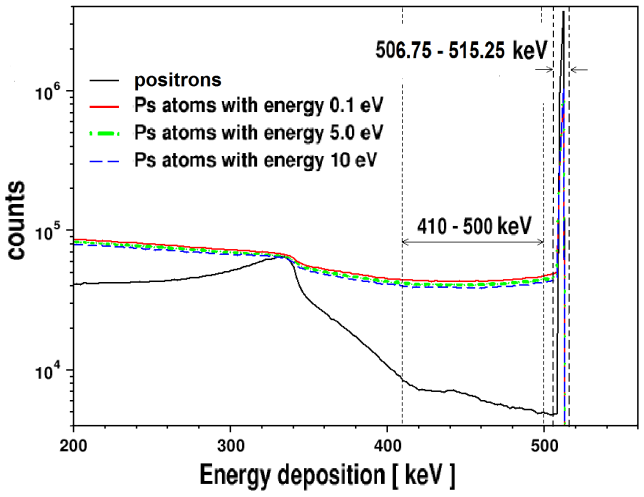

FIG. 12. Energy spectra deposition inside the HPGe detector given by annihilation photons of 10^8 Ps emitted with 0.1 eV (red), 5 eV (green dash-dotted line) and 10 eV (blue dashed line). The energy deposition spectrum given by the annihilation of 10^8 positrons in the target is also shown (black line). The experimental energy windows used for the valley region (410-500 keV) and peak region (506.75-515.25 keV) are indicated as dashed boxes.

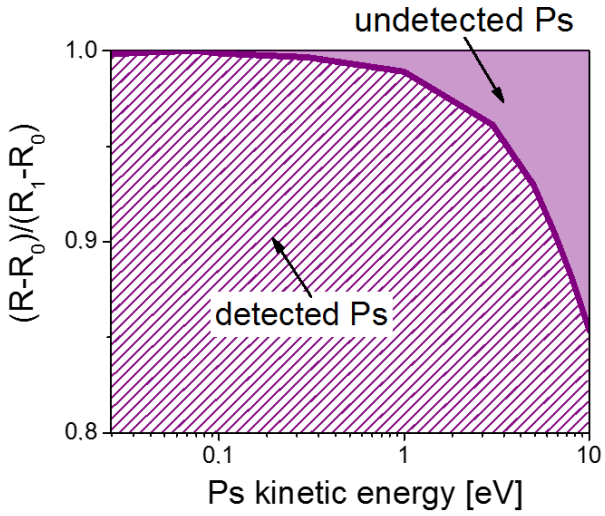

FIG. 13. $(R - R_0)/(R_1 - R_0)$ curve as a function of the Ps kinetic energy, E_{Ps}. The parallel lines pattern marks the detected o-Ps fraction while the homogeneous color marks the undetected o-Ps fraction

From the Monte-Carlo simulation is not possible to calculate the $F_{3\gamma}(E)$ fraction to be compared with data of Fig.7 and 9 because the Monte-Carlo would need as input the number and the energy distribution of Ps atoms reaching the back surface of the membrane and emitted into vacuum at each positron implantation energy.

As said in Sec.III.D, such information as a function of the positron implantation energy cannot be extracted from the measurements. Nevertheless, a rough indication about the kinetic energy of Ps emitted in transmission from our targets can be achieved. Indeed, the simulation in Fig.13 points out that the fraction of undetected Ps is null for kinetic energy lower than around 1 eV and it quickly increases only above this value. Let us now look at the experimental measurements taking into account this finding. If we consider, for example, the panel d) of Fig.7, we can see that the fraction of undetected o-Ps is negligible up to $E = 9\ keV$ and it increases only above that positron implantation energy. This indicates that the overall emitted o-Ps in transmission from the target 3.5 μm thick at $E < 9\ keV$ (at least 9 % of the implanted positrons) has a kinetic energy lower than 1 eV. Above $E = 9\ keV$, the undetected fraction quickly increases pointing out the presence of an increasing amount of forward emitted Ps faster than 1 eV. The same reasoning can be done for the other targets (with the exception of the 7.7 μm samples where the *measured amounts* are quite faint at the energy E at which the fraction of undetected o-Ps is no more negligible; panels a) of Fig.7 and Fig.9). The amount of forward emitted Ps with the entire kinetic energy distribution below 1 eV is ~ 4 % both in 5.0 μm and 6.3 targets for $E = 11\ keV$ and 12 keV, respectively. In the 5.0 μm re-etched target, the fraction of forward emitted Ps slower than 1 eV is at least ~ 5 % at $E = 13\ keV$.

[1] M. Deutsch, Phys. Rev. **82**, 455 (1951).

[2] S. Berko and H. N. Pendleton, Annual Review of Nuclear and Particle Science **30**, 543 (1980).

[3] A. Rich, Rev. Mod. Phys. **53**, 127 (1981).

[4] N. Prantzos, C. Boehm, A. M. Bykov, R. Diehl, K. Ferrière, N. Guessoum, P. Jean, J. Knoedlseder, A. Marcowith, I. V. Moskalenko, et al., Rev. Mod. Phys. **83**, 1001 (2011).

[5] D. Cassidy, Europ. Phys. J. D **72** (2018).

[6] A. Mills, Positron Solid State Physics, W. Brandt, A. Dupasquier (Eds.), Amsterdam, North-Holland (1983).

[7] K. Lynn, Positron Solid State Physics, W. Brandt, A. Dupasquier (Eds.), Amsterdam, North-Holland (1983).

[8] R. Brusa and A. Dupasquier, Physics with many positrons, A. Dupasquier, AP Mills, RS Brusa, IOS press Amsterdam, Oxford, Tokio, Washington DC (2010).

[9] S. Van Petegem, C. Dauwe, T. Van Hoecke, J. De Baerdemaeker, and D. Segers, Phys. Rev. B **70**, 115410 (2004).

[10] Y. Nagashima, Y. Morinaka, T. Kurihara, Y. Nagai, T. Hyodo, T. Shidara, and K. Nakahara, Phys. Rev. B **58**, 12676 (1998).

[11] S. Mariazzi, L. Toniutti, N. Patel, and R. S. Brusa, Applied Surface Science **255**, 191 (2008).

[12] D. B. Cassidy, P. Crivelli, T. H. Hisakado, L. Liszkay, V. E. Meligne, P. Perez, H. W. K. Tom, and A. P. Mills, Phys. Rev. A **81**, 012715 (2010).

[13] L. Liszkay, F. Guillemot, C. Corbel, J.-P. Boilot, T. Gacoin, E. Barthel, P. Pérez, M.-F. Barthe, P. Desgardin, P. Crivelli, et al., New Journal of Physics **14**, 065009 (2012).

[14] S. Mariazzi, P. Bettotti, S. Larcheri, L. Toniutti, and R. S. Brusa, Phys. Rev. B **81**, 235418 (2010).

[15] S. Mariazzi, P. Bettotti, and R. S. Brusa, Phys. Rev. Lett. **104**, 243401 (2010).

[16] T. Chang, M. Xu, and X. Zeng, Physics Letters A **126**, 189 (1987).

[17] R. S. Vallery, P. W. Zitzewitz, and D. W. Gidley, Phys. Rev. Lett. **90**, 203402 (2003).

[18] K. Ito, R.-S. Yu, K. Sato, K. Hirata, Y. Kobayashi, T. Kurihara, M. Egami, H. Arao, A. Nakashima, and M. Komatsu, J. of App. Phys. **98**, 094307 (2005).

[19] H. K. M. Tanaka, T. Kurihara, and A. P. Mills, J. of Phys.: Cond. Matt. **18**, 8581 (2006).

[20] C. He, T. Ohdaira, N. Oshima, M. Muramatsu, A. Kinomura, R. Suzuki, T. Oka, and Y. Kobayashi, Phys. Rev. B **75**, 195404 (2007).

[21] S. Mariazzi, R. Caravita, C. Zimmer, B. Rienäcker, A. Camper, A. Belov, G. Bonomi, R. S. Brusa, F. Castelli, G. Consolati, et al. (AEgIS), J. of Phys. B **54** (2021).

[22] S. L. Andersen, R. R. Johansen, J. B. Overgaard, J. K. Mortensen, K. K. Andersen, H. D. Thomsen, M. D. Lund, J. Chevallier, H. Knudsen, and U. I. Uggerhj, Europ. Phys. J. D **68** (2014).

[23] S. L. Andersen, D. B. Cassidy, J. Chevallier, B. S. Cooper, A. Deller, T. E. Wall, and U. I. Uggerhøj, J. of Phys. B **48**, 204003 (2015).

[24] S. L. Andersen, Ph.D. thesis, Aarhus University (2015), URL `http://pure.au.dk/portal/files/90669596/thesisSLAndersen.pdf`.

[25] M. H. Weber, S. Tang, S. Berko, B. L. Brown, K. F. Canter, K. G. Lynn, A. P. Mills, L. O. Roellig, and A. J. Viescas, Phys. Rev. Lett. **61**, 2542 (1988).

[26] N. Zafar, G. Laricchia, M. Charlton, and A. Garner, Phys. Rev. Lett. **76**, 1595 (1996).

[27] A. P. Mills and W. S. Crane, Phys. Rev. A **31**, 593 (1985).

[28] K. Michishio, L. Chiari, F. Tanaka, N. Oshima, and Y. Nagashima, Review of Scientific Instruments **90**, 023305 (2019).

[29] T. S. Pedersen, J. R. Danielson, C. Hugenschmidt, G. Marx, X. Sarasola, F. Schauer, L. Schweikhard, C. M. Surko, and E. Winkler, New J. of Phys. **14**, 035010 (2012).

[30] A. Mills and M. Leventhal, Nucl. Inst. and Meth. B **192**, 102 (2002).

[31] M. Oberthaler, Nucl. Inst. and Meth. B **192**, 129 (2002).

[32] P. Crivelli, D. A. Cooke, and S. Friedreich, Int. J. of Mod. Phys.: Conf. Ser. **30** (2014).

[33] D. B. Cassidy and S. D. Hogan, Int. J. of Mod. Phys.: Conf. Ser. **30**, 1460259 (2014).

[34] S. Mariazzi, R. Caravita, M. Doser, G. Nebbia, and R. S. Brusa, Europ. Phys. J. D **74** (2020).

[35] M. Charlton, Phys. Lett. A **143**, 143 (1990).

[36] M. Doser, C. Amsler, A. Belov, G. Bonomi, P. Brunig, J. Bremer, R. Brusa, G. Burkhart, L. Cabaret, C. Canali, et al. (AEgIS Collaboration), Classical and Quantum

Gravity **29**, 184009 (2012).
[37] C. Amsler, M. Antonello, A. Belov, G. Bonomi, R. S. Brusa, M. Caccia, A. Camper, R. Caravita, F. Castelli, P. Cheinet, et al. (AEgIS Collaboration), Comm. Phys **4**, 1 (2021).
[38] S. Aghion, C. Amsler, T. Ariga, G. Bonomi, R. S. Brusa, M. Caccia, R. Caravita, F. Castelli, G. Cerchiari, D. Comparat, et al. (AEgIS Collaboration), Nucl. Inst. and Meth. B **407**, 55 (2017).
[39] M. Ghulinyan, C. J. Oton, Z. Gaburro, P. Bettotti, and L. Pavesi, App. Phys. Lett. **82**, 1550 (2003).
[40] J. Álvarez, P. Bettotti, I. Suárez, N. Kumar, D. Hill, V. Chirvony, L. Pavesi, and J. Martínez-Pastor, Opt. Express **19**, 26106 (2011).
[41] N. Kumar, S. Gennaro, P. Sasikumar, G. Sorar, and P. Bettotti, Appl. Phys. A **116**, 251 (2014).
[42] O. Bisi, S. Ossicini, and L. Pavesi, Surface Science Reports **38**, 1 (2000).
[43] R. Guider, C. Traversa, and P. Bettotti, Opt. Mater. Express **5**, 2128 (2015).
[44] A. Zecca, M. Bettonte, J. Paridaens, G. P. Karwasz, and R. S. Brusa, Meas. Sci. and Tech. **9**, 409 (1998).
[45] R. S. Brusa, C. Macchi, S. Mariazzi, and G. P. Karwasz, Acta Phys. Pol. A **107**, 702 (2005).
[46] A. P. Mills, Phys. Rev. Lett. **41**, 1828 (1978).
[47] E. Soininen, A. Schwab, and K. G. Lynn, Phys. Rev. B **43**, 10051 (1991).
[48] M. Eldrup, A. Vehanen, P. J. Schultz, and K. G. Lynn, Phys. Rev. B **32**, 7048 (1985).
[49] S. Valkealahti and R. Nieminen, Appl. Phys. A **35**, 51 (1984).
[50] E. Soininen, J. Mäkinen, D. Beyer, and P. Hautojärvi, Phys. Rev. B **46**, 13104 (1992).
[51] J. Dryzek and P. Horodek, Nucl. Inst.and Meth. in Phys. B **266**, 4000 (2008), ISSN 0168-583X.
[52] J. Algers, P. Sperr, W. Egger, G. Kögel, and F. H. J. Maurer, Phys. Rev. B **67**, 125404 (2003).
[53] F. Guatieri, S. Mariazzi, and R. S. Brusa, Europ. Phys. J. D **72** (2018).
[54] P. J. Schultz and K. G. Lynn, Rev. Mod. Phys. **60**, 701 (1988).
[55] J. Schindelin, I. Arganda-Carreras, E. Frise, V. Kaynig, M. Longair, T. Pietzsch, S. Preibisch, C. Rueden, S. Saalfeld, B. Schmid, et al., Nat. Meth. **9**, 676 (2012).
[56] D. E. Aspnes and A. A. Studna, Phys. Rev. B **27**, 985 (1983).
[57] M. P. Petkov, C. L. Wang, M. H. Weber, K. G. Lynn, and K. P. Rodbell, J. of Phys. Chem. B **107**, 2725 (2003).
[58] P. Bettotti, Springer Handbook of Nanomaterials pp. 883–902 (2013).
[59] D. B. Cassidy, T. H. Hisakado, V. E. Meligne, H. W. K. Tom, and A. P. Mills, Phys. Rev. A **82**, 052511 (2010).
[60] S. Aghion, C. Amsler, A. Ariga, T. Ariga, A. Belov, G. Bonomi, P. Brunig, J. Bremer, R. S. Brusa, L. Cabaret, et al. (AEgIS Collaboration), Nucl. Inst. and Meth. B **362**, 86 (2015).
[61] K. Dulski, S. D. Bass, J. Chhokar, N. Chug, C. Curceanu, E. Czerwiski, M. Dagdar, J. Gajewski, A. Gajos, M. Gorgol, et al., Nucl. Inst. and Meth. A **1008**, 165452 (2021).
[62] W. Krzemien, A. Gajos, K. Kacprzak, K. Rakoczy, and G. Korcyl, SoftwareX **11**, 100487 (2020).
[63] M. Antonello, A. Belov, G. Bonomi, R. S. Brusa, M. Caccia, A. Camper, R. Caravita, F. Castelli, D. Comparat, G. Consolati, et al. (AEgIS Collaboration), Phys. Rev. A **102**, 013101 (2020).